ARTICLES SCIENCE CHINA Materials

mater.scichina.com link.springer.com

Published online 7 November 2017 | https://doi.org/10.1007/s40843-017-9113-1

Sci China Mater 2018, 61(1): 80–90

Cobalt-vanadium bimetal-based nanoplates for efficient overall water splitting

Yinglu Xiao, Chungui Tian*, Mei Tian, Aiping Wu, Haijing Yan, Congfang Chen, Lei Wang, Yanqing Jiao and Honggang Fu*

ABSTRACT **The development of effective and low-cost catalysts for overall water splitting is essential for clean production of hydrogen from water. In this paper, we report the synthesis of cobalt-vanadium (Co-V) bimetal-based catalysts for the effective water splitting. The $Co_2V_2O_7{\cdot}xH_2O$ nanoplates containing both Co and V elements were selected as the precursors. After the calcination under NH_3 atmosphere, the Co_2VO_4 and Co/VN could be obtained just by tuning the calcination temperature. Electrochemical tests indicated that the Co-V bimetal-based materials could be used as active hydrogen evolution reaction (HER) and oxygen evolution reaction (OER) catalyst by regulating their structure. The Co/VN showed good performance for HER with the onset potential of 68 mV and can achieve a current density of 10 mA cm^{-2} at an overpotential of 92 mV. Meanwhile, the Co_2VO_4 exhibited the obvious OER performance with overpotential of 300 mV to achieve a current density of 10 mA cm^{-2}. When the Co_2VO_4 and Co/VN were used as the anode and cathode in a two-electrode system, respectively, the cell needed a voltage of 1.65 V to achieve 10 mA cm^{-2} together with good stability. This work would be indicative to constructing Co-V bimetal-based catalysts for the catalytic application.**

Keywords: water splitting, electrocatalysis, Co_2VO_4, Co/VN

INTRODUCTION

Economic development results in the increased demand for the production and storage of clean energy. Hydrogen, with zero CO_2 emission in use, has attracted intensive attention as clean energy resources [1]. Today, most H_2 is produced from fossil resources through a steam reforming process, which consumes the fossil fuels accompanied by the emission of CO_2 [2,3]. The electrocatalytic water splitting has been considered as a promising approach for sustainable hydrogen production from clean and abundant water with zero carbon emission [4]. The theoretical cell voltage for water splitting is 1.23 V at 298 K ($\Delta E^0_{rev,298}$=1.23 V) [5,6]. However, a large overpotential is required to overcome the kinetic barrier induced by the high activation energy, and thus to form the reaction intermediates in the system, whatever for an anodic oxygen evolution reaction (OER) and a cathodic hydrogen evolution reaction (HER) [7]. For the practical water spitting, the effective catalysts are needed to decrease the overpotential of the reaction, thus making the process more energy-efficient [8–10]. In this regard, the state-of-the art precious metals (Pt, IrO_2, RuO_2) for OER and HER have suffered from the high price and lack of reserves, thus limiting their applications for the overall water splitting [11–13].

The materials based on early and late transition metals (ETMs and LTMs) are promising for HER and OER [14,15], such as the transition metals sulfides [16,17], phosphides [18–22], selenide [23], nitride [24–26] and carbides [27] for HER, and oxides (Ni oxides [28,29] and Co oxides [30–32]) for OER. The cobalt (Co), as a typical LTM, is promising in HER due to its relatively low cost and the activity for the reduction of H^+ [33]. Generally, single Co metals have shown poor activity and stability for HER. To achieve improved performance, the Co-based hybrids need to be constructed. For example, Co-doped carbon flakes [34], Co-doped MoO_2 nanowires [35], Co doped CNTs [36] and TiO_2-Co NTs [37] have been used as good catalysts for HER. On the other hand, the vanadium (V), as a typical ETM, has been intensively studied in catalytic and energy fields. The VN and VC are demonstrated to be useful for HER [38], while VOOH are active for OER [39]. The good conductivity and stability of VN are also favorable for its application either as catalyst or as support. It is shown that the combination of oxides with V and Co can result in OER active catalysts [40–42]. Also, the effective combination of early and late

Key Laboratory of Functional Inorganic Material Chemistry, Ministry of Education, Heilongjiang University, Harbin 150080, China

* Corresponding authors (emails: chunguitianhq@163.com (Tian C); fuhg@vip.sina.com, fuhonggang@hlju.edu.cn (Fu H))

TMs is useful for designing the advanced materials [43–45]. It is possible and promising to develop a simple and effective way to construct the Co-V based catalyst for HER and OER.

Here, we reported the rational combination of V and Co toward the effective electrocatalysts. By simply tuning the synthetic parameters, the active OER and HER catalysts based on Co-V bimetals can be obtained. The $Co_2V_2O_7{\cdot}xH_2O$ nanoplates containing both Co and V elements were selected as a precursor. After the calcination under NH_3 atmosphere, the Co_2VO_4 and Co/VN can be selectively obtained just by tuning the calcination temperature. Electrochemical tests indicate that the Co-V bimetal-based materials are active catalysts for HER and OER. Specifically, the Co/VN from the calcination at 500°C showed good performance for HER with the onset potential of 68 mV and can achieve a current density of 10 mA cm^{-2} at an overpotential of 92 mV. Meanwhile, the Co_2VO_4 from calcination at 400°C can be used as active OER catalyst with overpotential of 300 mV to achieve a current density of 10 mA cm^{-2}. When the Co_2VO_4 and Co/VN were used as the cathode and anode in a two-electrode system, respectively, the cell needs a voltage of 1.65 V to achieve 10 mA cm^{-2} together with good stability.

EXPERIMENT SECTION

Materials and chemicals

Ammonium vanadate (NH_4VO_3), cobalt chloride hexahydrate ($CoCl_2{\cdot}6H_2O$) and hexamethynetetramine ($C_6H_{12}N_4$, HMT) were all purchased from Aladdin Chemical Reagent Co. Ltd. All of the reagents were of analytical grade and used without any further purification. Deionized water was used throughout the experiments.

Synthesis of $Co_2V_2O_7{\cdot}xH_2O$ nanoplates

The $Co_2V_2O_7{\cdot}xH_2O$ precursor was synthesized according to a previous method with some modifications. In detail, 0.94 g of NH_4VO_3, 0.38 g of $CoCl_2{\cdot}6H_2O$ were dissolved in mixed solvent of 140 mL deionized water and 20 mL ethylene glycol at 80°C under vigorous stirring to form a clear solution. Then, 2.8 g of $C_6H_{12}N_4$ was added into the above solution. After stirring continually for 4 h, the solids were collected by centrifugation, rinsed with distilled water and ethanol for several times, and finally dried overnight in oven.

Synthesis of Co-V bimetal-based nanoplates

The Co/VN nanosheets were prepared by calcinating the $Co_2V_2O_7{\cdot}xH_2O$ precursor under NH_3 at 500°C for 3 h in a tube furnace. By varying the calcination temperature, the products with different components were prepared. Typically, the Co_2VO_4 and Co_3V/VN were prepared by calcinating the precursor at 400°C and 600°C, respectively (see Table S1).

Materials characterization

The X-ray powder diffraction (XRD) patterns were collected on Bruker D8 Focus (Cu Kα radiation, λ=1.5406 Å) with an accelerating voltage of 40 kV. Transmission electron microscopy (TEM, JEM-2100, 200 kV) and scanning electron microscopy (SEM, Hitachi S-4800, 5 kV) were used to characterize the morphology and size of the samples. X-ray photoelectron spectroscopy (XPS) test was performed on VG ESCALAB MK II using an MgKa (1253.6 eV) achromatic X-ray radiation. The specific surface area of the samples was tested on a Micromeritics Tristar II and calculated by the Brunauer-Emmett-Teller (BET) method.

Electrode preparation and electrochemical measurements

The catalyst ink was typically made by dispersing 5 mg of the catalyst and 0.5 mg carbon black in 1 mL water/ethanol mixture (v/v=1:1). The carbon black was added to increase electrical conductivity of the catalyst. After adding 20 μL of 5 wt.% of Nafion solution and ultrasonication, an aliquot of 10 μL was pipetted onto the work electrode (0.07065 cm^2 in area). Electrochemical tests were performed on a BAS100B electrochemical workstation. The OER and HER tests were carried out using a three-electrode configuration composed of a reference electrode (saturated calomel electrode, SCE), an auxiliary electrode (graphite rod) and the working electrode (glassy carbon electrode, GCE). The overall water splitting was conducted across the two electrodes. The Co_2VO_4 and Co/VN catalysts were drop-casted onto a Ni foam (1 cm×1 cm) and used as the anode and cathode, respectively. All the potentials were referenced to reversible hydrogen electrode (RHE) according to the equation: $E_{RHE}=E_{SCE}+0.242\ V+0.059pH$. Polarization data was collected in 1 mol L^{-1} KOH (pH 13.8) with the scan rate of 5 mV s^{-1} on GCE under 1600 rpm. The electrochemically active surface area (ECSA) of the catalysts modified electrodes were calculated using the double-layer capacitor based on the reported electrochemical method. Electrochemical impedance spectroscopy (EIS) was measured at the open-circuit voltage from 100 kHz to 0.1 Hz with a 5 mV AC dither. The cyclic voltammograms (CVs) were tested with different rates from 40 to 140 mV s^{-1}. Long-term stability tests were carried out at 100 mV s^{-1}. The pH of the solution was measured before

and after testing, and no obvious change was observed. All the potentials in the polarization curves and Tafel plots were internal resistance (*iR*) compensated. The data for the two electrode systems were recorded without *iR* compensation. All of the tests were performed at room temperature.

Determination of TOF value

The active surface redox sites of the materials were determined by integrating the oxidation peak without the capacitive current. Further, the active area (*S*) divided by the scanning rate gives the integrated charge of the peak Q_S [46]:

$$Q_S = \frac{S}{0.02(\mathrm{V/s})}. \quad (1)$$

To calculate the turnover frequency (TOF), we used the following formula:

$$\mathrm{TOF} = \frac{j(\mathrm{A})}{nQ_S}. \quad (2)$$

RESULTS AND DISCUSSION

Material preparation and characterizations

Scheme 1 presents the preparation procedure of the Co-V bimetal-based catalyst. The $Co_2V_2O_7{\cdot}xH_2O$ precursor nanoplates are produced by a low-temperature solution-phase method. During the calcination under NH_3 atmosphere, the $Co_2V_2O_7{\cdot}xH_2O$ precursor underwent a series of transformation. At lower temperature (400°C), the V^{5+} in $Co_2V_2O_7{\cdot}xH_2O$ are partially reduced to V^{4+}, and thus the Co_2VO_4 could be obtained. With the increase of the calcination temperature to 500°C, the V was further reduced and combined with N to from the VN accompanied by the reduction of Co^{2+} to Co metal, resulting in the formation of Co/VN hybrid. Both Co and V are from the single source of $Co_2V_2O_7{\cdot}xH_2O$ precursor, thus the intimate contact of Co and VN can be realized. The tight bonding of Co with VN is favorable to preventing the Co particles from aggregation, thus producing a large number of stable and exposed active sites.

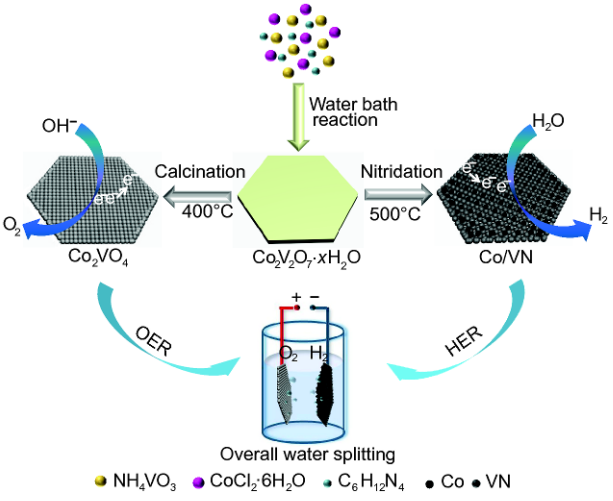

Scheme 1 Schematic illustration for the formation of Co-V bimetal-based catalysts.

The first step in the synthesis of Co-V bimetal-based catalyst is the preparation of the $Co_2V_2O_7{\cdot}xH_2O$ precursor with uniform size and morphology. The precursor was characterized by XRD, SEM and TEM methods. The XRD pattern of $Co_2V_2O_7{\cdot}xH_2O$ is shown in Fig. 1a. The peaks match well with the XRD result of $Co_2V_2O_7{\cdot}xH_2O$ reported previously [47]. The morphology and size of the precursor were studied by SEM and TEM. From the SEM image (Fig. 1b), we can see the hexagonal plates with uniform size and regular morphology. The $Co_2V_2O_7{\cdot}\ xH_2O$

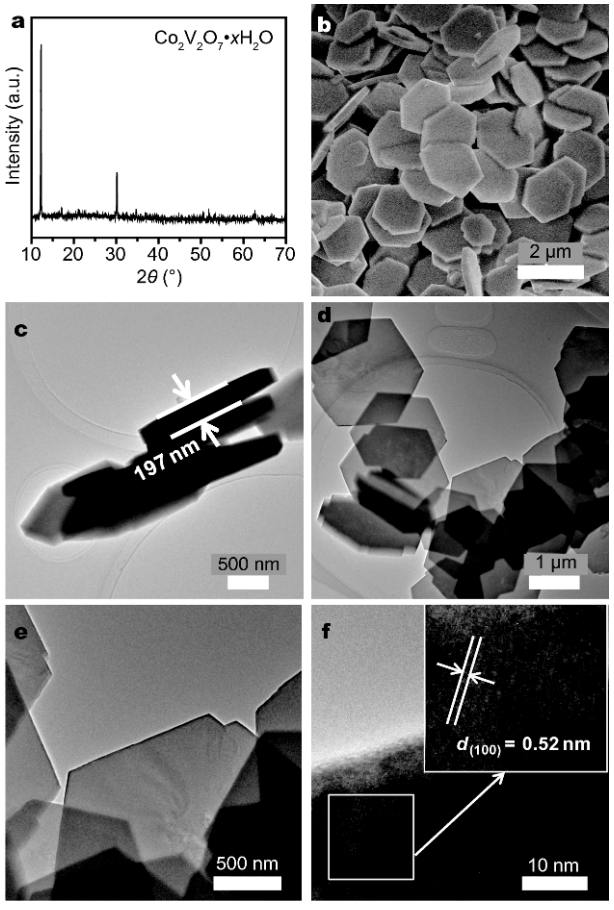

Figure 1 (a) XRD pattern; (b) SEM image; (c–f) TEM images of the $Co_2V_2O_7{\cdot}xH_2O$ precursor nanoplates. The inset in (f) is the HRTEM image of the selected area.

nanoplates have smooth surface with a thickness about 200 nm. The low-magnification TEM images (Fig. 1c, d) further indicate the formation of the quasi-hexagonal plates. Several vertical plates can be distinctly observed in Fig. 1c. We can estimate the thickness of the plates to be about 200 nm. The plates have smooth surface, consistent with the result of SEM. The high-resolution TEM (HRTEM) image (Fig. 1f) shows the fringe spacing of 0.52 nm, which is corresponded to the previous reports about $Co_2V_2O_7{\cdot}xH_2O$ [47,48]. The above tests demonstrated the successful preparation of the $Co_2V_2O_7{\cdot}xH_2O$ precursor with uniform size and morphology.

The $Co_2V_2O_7{\cdot}xH_2O$ precursor was calcinated under NH_3 atmosphere to produce Co-V bimetal-based electrocatalysts. Fig. 2a shows the XRD patterns of Co/VN sample from the calcination at 500°C. The diffraction patterns corresponding to VN (JCPDS No.25-1252) and metallic Co (JCPDS No.15-0806) can be observed, implying the formation of Co/VN. It is shown that the formation of the V–N bond at 500°C is easier than the Co–N bond. At the lower temperature, the metallic Co is preferentially formed by reducing the corresponding oxides with ammonia [49]. So, by controlling the synthetic parameters, we can prepare the composites of Co combined with VN. After nitridation, the nanosheets morphology is well retained as shown in the SEM image (Fig. 2b). However, the surface becomes rough with many nanoparticles embedded in the sheets, different with the smooth surface of $Co_2V_2O_7{\cdot}xH_2O$ precursor. The Co nanoparticles are segregated on the nanosheets surface. Also, the pore can be observed on the nanosheets. The existence of pores can provide fast transportation paths for the electrolytes, which is favorable to improving the catalytic performance. The TEM images can give further information about the micro-structure of Co/VN. The low-magnified TEM image in Fig. 2c indicates the uniform plate-like structure. Many small particles can be observed on porous plate-like substrate, obviously different with original $Co_2V_2O_7{\cdot}xH_2O$ precursor. The HRTEM image shows the lattice fringe spacing of 0.238 nm, corresponding to (111) crystal plane of VN (JCPDS No.25-1252) and lattice fringe of 0.208 nm associated with the (111) crystal plane of metallic Co (JCPDS No.15-0806) in the areas of two neighboring particles (Fig. 2f). The above results confirm the formation of Co/VN composite with intimate interface contact, which can be ascribed to the fact that both Co and V are from the single source of $Co_2V_2O_7{\cdot}xH_2O$ precursor.

XPS was conducted to determine the elements in Co/VN and their corresponding valence. As shown in Fig. 3a,

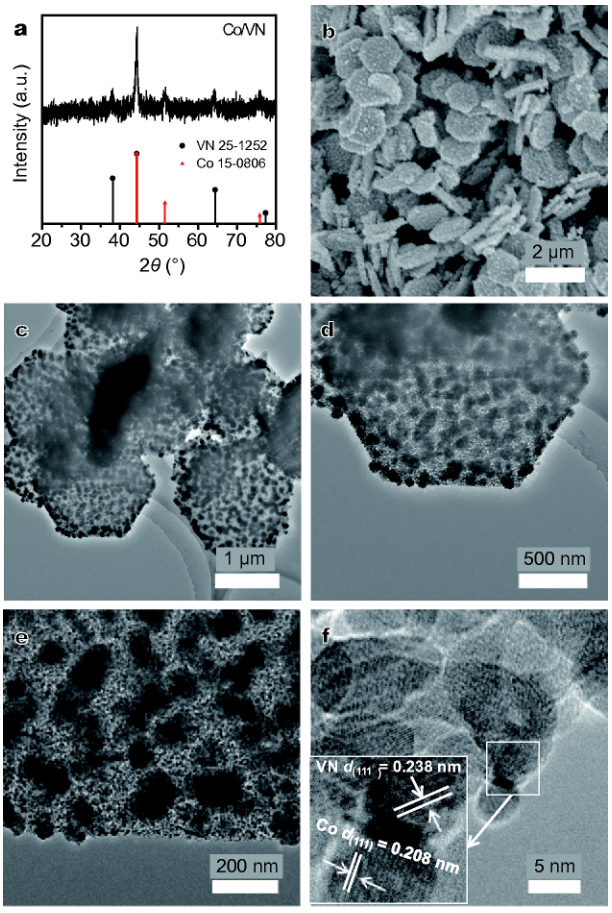

Figure 2 (a) XRD pattern; (b) SEM image; (c–f) TEM images of Co/VN. The inset in (f) is an HRTEM image.

the survey spectrum shows the presence of Co 2p, V 2p, O 1s, C 1s and N 1s peaks. The Co $2p_{3/2}$ XPS (Fig. 3b) can be attributed to metallic Co, cobalt oxides (Co^{2+} and Co^{3+}) and satellite signals. The high-resolution V $2p_{3/2}$ peak (Fig. 3c) can be fitted with three peaks located at 514.07, 515.3 and 516.7 eV, corresponding to V–N, V–O–N and V–O, respectively [49,50]. The oxygen-containing species (V–O, V–O–N) should stem from the slight surface oxidation of VN. The presence of Co^{2+} and Co^{3+} are due to the slight surface oxidation of Co particles [49]. Fig. 3d displays high-resolution N 1s XPS spectra, in which the peak at 396.4 eV is the typical characteristic of metal nitrides [51], while the other at 397–402 eV can be assigned to the N bonding to the oxide. The results suggest that Co nanoparticles are embedded in the porous VN nanosheets.

The Co-V bimetallic samples were synthesized by nitriding the $Co_2V_2O_7{\cdot}xH_2O$ under NH_3 atmosphere. The NH_3 can act as reducing agent and nitridation agent, and the ability can be largely affected by the calcination

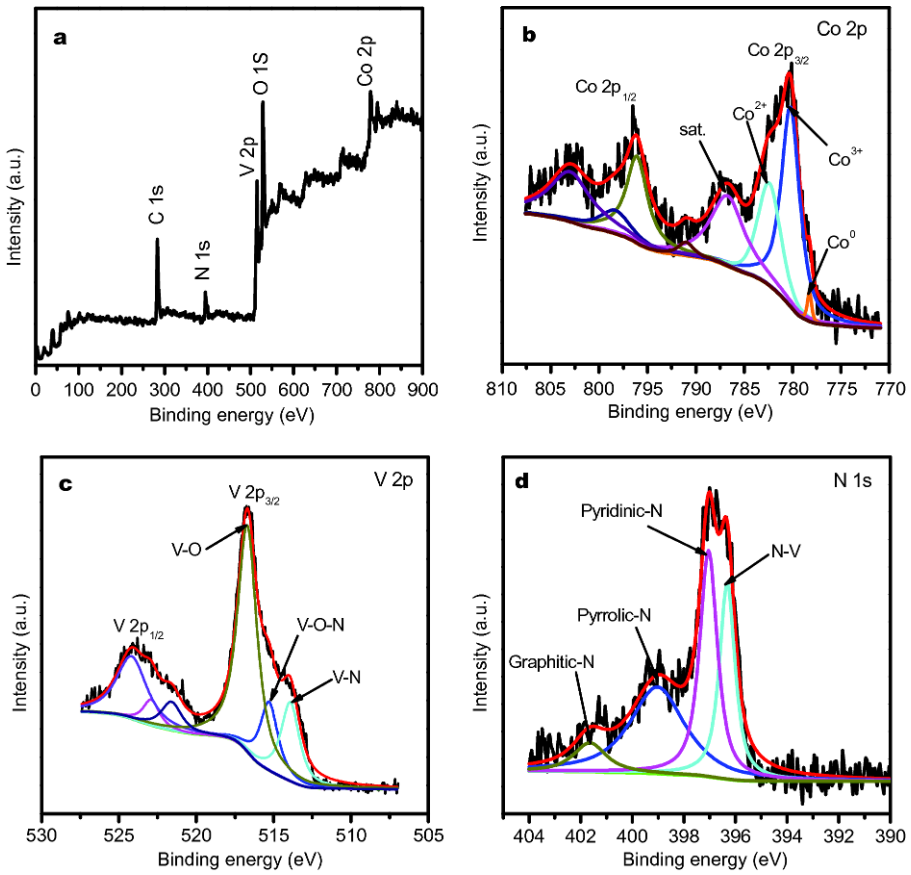

Figure 3 (a) The XPS survey spectrum; (b–d) high resolution spectra of Co 2p, V 2p and N 1s of Co/VN hybrid.

temperature. In order to explore the influence of temperature, the precursor was calcinated at 400°C and 600°C, besides the 500°C. The peaks in the precursor cannot be observed after the calcination at 400°C. In this case, all the peaks can be indexed to the standard patterns of Co_2VO_4 (JCPDS No.73-1633) (Fig. S1a). The results indicate that V^{5+} in precursor is reduced to V^{4+} in Co_2VO_4 and the NH_3 plays the role as reducing agent at lower temperature. The increase in temperature will result in enhanced ability of NH_3 as nitridation agent, leading to the formation of Co/VN composites at 500°C. Further elevating the temperature to 600°C, the precursor is completely transformed into composites composed of Co_3V (JCPDS No.65-7040) and VN (JCPDS No.65-9409), as demonstrated by XRD (Fig. S1b). From the SEM image (Fig. S2), we can observe the nanoplates composed of numerous small subunits with the accumulated pore. From Fig. S3, it can be seen that the Co_3V/VN sample remains hexagonal plate-like structure composed of the nanoparticles. The surface of the plate is rougher with the larger particle size than that of Co/VN and Co_2VO_4. The increase in size should be ascribed to the high calcination temperature. The temperature-dependent experiments indicate that Co-V bimetal-based nanoplates with adjusted components can be selectively prepared by simply tuning the calcination parameters of $Co_2V_2O_7{\cdot}xH_2O$ precursor.

The tuning of components can be further supported by XPS test. Fig. S4 shows the XPS spectra of the Co_2VO_4. The survey spectrum shows the presence of Co 2p, V 2p and O 1s in the sample (Fig. S4a). The high resolution peak of Co 2p (Fig. S4b) can be fitted to Co^{2+} (781.06 and 796.9 eV) [52,53]. In addition, two peaks located at 516.7 and 524.02 eV can be observed in the V $2p_{3/2}$ region, attributed to V^{4+} (Fig. S4c) [52]. The broad peak of O 1s (Fig. S4d) can be fitted by three peaks at binding energies of 531.8, 530.74 and 530.06 eV. The stronger peak located at 530.06 eV can be referred to the lattice oxygen in the metal oxide (O_L), and the other peaks at approximately 530.74 and 531.8 eV suggests the presence of hydroxyl species (O_H) and adsorbed water on the surface (O_a). For Co_3V/VN, the survey spectrum also shows the presence of

Co 2p, V 2p, O 1s and N 1s (Fig. S5a). The Co $2p_{3/2}$ XPS (Fig. S5b) can be divided into four peaks at 782.0, 780.2, 778.2 and 786.9 eV, attributed to Co^{2+}, Co^{3+}, alloy Co and satellite signals. The Co^{2+} and Co^{3+} are from the slight surface oxidation of alloy in air [49]. The V $2p_{3/2}$ peak (Fig. S5c) can be fitted with four peaks at 513.4, 514.1, 515.3, and 517.2 eV, corresponding to alloy V, V–N, V–O–N and V–O, respectively. The alloy V has higher binding energy than the V^0 (512.3 eV) [51], maybe due to the electron transfer between V and Co in the alloys [54,55]. Fig. S5d displays the N 1s XPS spectrum, the presence of N with dominant N–V bond can be observed, in which the peak at 396.4 eV is characteristic of metal nitrides, while the peak located at around 398 eV is assigned to the nitrogen bonding to the oxide.

Electrochemical performance for HER

The HER activity was evaluated using a three-electrode cell in 1 mol L^{-1} KOH. Before the test, the SCE was calibrated referenced to RHE. All the potentials in the polarization curves and Tafel plots are *iR* compensated. Besides, the polarization curves without *iR* compensation are shown in Fig. S6. The polarization curves of Co_2VO_4, Co/VN, Co_3V/VN and commercial Pt/C are displayed in Fig. 4a, and the corresponding data are listed in Table S2. We can see that the Pt/C shows the expected good activity with onset potential about 0 mV. Also, all Co-V bimetal samples show the obvious HER activity. Among them, the Co/VN shows a small onset potential of 62 mV (*vs.* RHE, all the potentials are referenced to RHE in this work). At a current density of 10 mA cm^{-2}, Co/VN gives an overpotential of only 92 mV, which is much lower than that of common HER electrocatalysts, such as Co-N-MoO_2 (258 mV) [35], VS/Ni_xS_y/NF (233 mV) [44], VC-NS (98 mV) [38], CoS_2/MoS_2/RGO (160 mV) [56] and Mo_2C/MoO_2 (315 mV) [57]. For Co_2VO_4 and Co_3V/VN, the overpotentials required to reach the current density of 10 mA cm^{-2} are about 205 and 136 mV, being worse than that of Co/VN. The HER kinetics of the catalysts is investigated based on Tafel slopes, which are determined from the Tafel plots in the linear portions. The Tafel plots can be fitted with the Tafel equation ($\eta=b\times\log j+a$, where j is the current density, b is the Tafel slope) as shown in Fig. 4b. Tafel slopes are about 68.68, 52.49, and 56.56 mV dec^{-1} for Co_2VO_4, Co/VN and Co_3V/VN, respectively. The Tafel slopes suggest that HER on Co-V bimetal-based catalyst undergoes Volmer-Heyrovsky mechanism, for which the reaction rate is determined by the electrodesorption step (H_2O discharge and desorption of H from the catalyst surface) [58]. The Co/VN shows the lowest Tafel slope values, implying its favorable kinetics for HER. We further measured the double layer capacitance (C_{dl}) by using a CV method to estimate the ECSA (Fig. S7). It is shown that the Co/VN shows the C_{dl} of 31.2 mF cm^{-2}, higher than Co_2VO_4 (22.1 mF cm^{-2}) and Co_3V/VN (27.8 mF cm^{-2}) as depicted in Fig. 4c. The high ECSA further suggests the good performance of Co/VN. The different activity of Co-V catalysts should be related to their structure. The oxides usually have good activity for OER due to their favorable kinetics for the reduction of OH^-. Thus, the Co_2VO_4 has shown relatively high onset potentials for HER. The Co is active catalyst for HER. The combination of the small size of Co and suitable conductivity of VN leads to the good activity of Co/VN. The Co_3V/VN has shown worse activity than Co/VN due to the large particle size in the plates. The specific surface area and pore-size distribution of the nanosheets are shown in Fig. S8a. The analysis indicates that the Co/VN nanosheets show a larger surface area of 33.8 m^2 g^{-1} than the Co_2VO_4 (29.2 m^2 g^{-1}) and Co_3V/VN (12.0 m^2 g^{-1}) sample. At the same time, the dominating BJH pore-size is about 29.4 nm for Co/VN, greater than that of the Co_2VO_4 sample (5.2 nm), and less than that of the Co_3V/VN sample (72.6 nm) (Fig. S8b). The large surface area and well defined pore structure allow the inner active sites of the catalyst to be easily contacted with the electrolyte, which is highly desirable for electrochemical reaction. Since a large number of Co nanoparticles are embedded in the highly conductive VN layer, the electrons can be easily transported in the reaction, thus decreasing the contact resistance. The charge transfer resistance of the Co/VN was determined by EIS. The Nyquist plot of Co/VN (Fig. S9) shows a small charge transfer resistance (R_{ct}), indicating high conductivity and fast proton discharge kinetics of the Co/VN electrocatalyst. The durability of the Co/VN electrocatalyst was tested by CV at a scanning rate of 10 mV s^{-1}. The polarization curves show a little shift in the overpotential for a current density of 10 mA cm^{-2} in the initial 5000 CV scans. The inset in Fig. 4d shows the time dependence of the current density for Co/VN at an overpotential of 92 mV, also suggesting its good stability in long-term electrochemical test.

Electrochemical performance for OER

As shown above, the Co-V bimetal-based catalyst can act as active HER catalyst. It is shown that the materials containing Co and/or V (typically the oxides) are potential catalysts for OER [33]. We then studied the OER performance of the samples in 1 mol L^{-1} KOH. As shown

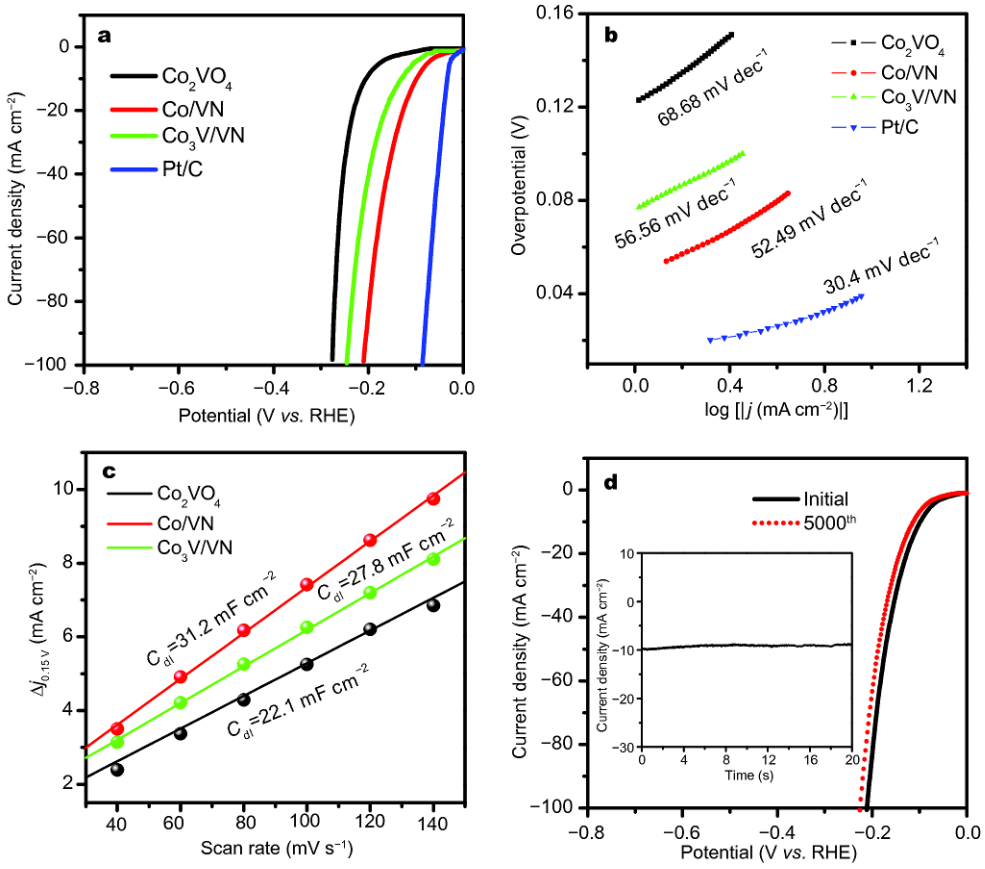

Figure 4 (a) Linear sweep voltammetry (LSV) curves for Co_2VO_4, Co/VN, Co_3V/VN and commercial Pt/C with *iR* compensation; (b) Tafel plots for Co_2VO_4, Co/VN, Co_3V/VN and Pt/C; (c) the capacitive current at 0.15 V of Co_2VO_4, Co/VN and Co_3V/VN; (d) polarization data for the Co/VN sample initially and after 5000 CV. The inset in (d) is the dependence of the current density for Co/VN at overpotential of 92 mV for 20 h.

in Fig. 5 and Fig. S10, all samples show the obvious activity for OER (Table S3). The Co_2VO_4 nanosheets exhibit good OER catalytic activity, which may be related to its characteristics as bimetal oxides. The slight surface oxidation of Co/VN and Co_3V/VN can also render the activity of the catalyst for OER [59]. Specifically, the overpotentials required to reach the current density of 10 mA cm^{-2} are 300 mV for Co_2VO_4, lower than 312 and 324 mV for Co/VN and Co_3V/VN (Fig. 5a). The value is also lower than those of $Co_3V_2O_8$ (359 mV) [40], FeNi-CoO_4 (350 mV) [60] and MnO_2/$NiCo_2O_4$ NF (340 mV) [61]. We can find that the RuO_2 shows the overpotential about 375 mV to reach a current density of 10 mA cm^{-2}. The Tafel slopes are found to be close to each other (65.32, 69.02, and 68.68 mV dec^{-1} for Co_2VO_4, Co/VN and Co_3V/VN, respectively), suggesting the similar OER kinetics (Fig. 5b). We thus measured the C_{dl} for the samples (Fig. S11). The ECSA of Co_2VO_4 sheets is 40.7 mF cm^{-2}, much larger than the Co/VN (20.3 mF cm^{-2}) and Co_3V/VN (15.5 mF cm^{-2}) (Fig. 5c). Turnover frequency (TOF) is another parameter to evaluate the activity of catalysts. The TOF values calculated at 370 mV are 1.09, 0.69 and 0.47 s^{-1} for Co_2VO_4, Co/VN and Co_3V/VN, respectively (Fig. S12, Table S4). The high TOF value of Co_2VO_4 implies its better activity than the other two samples. Besides the high activity, the Co_2VO_4 also shows good durability as confirmed by the continuous CV and the chronoamperometry measurements (Fig. 5d). The electrode exhibits stable performance with a little loss after 5000 CV cycles and can maintain a current density of 20 mA cm^{-2} with minimal change of overpotential upon a 12 h operation. The enhanced OER activities of Co_2VO_4 may be related to its characteristics as bimetal oxides, high surface active sites and plentiful pores.

The performance for overall water splitting

Considering the good catalytic ability and stability of Co_2VO_4 and Co/VN for the OER and HER, a two-elec-

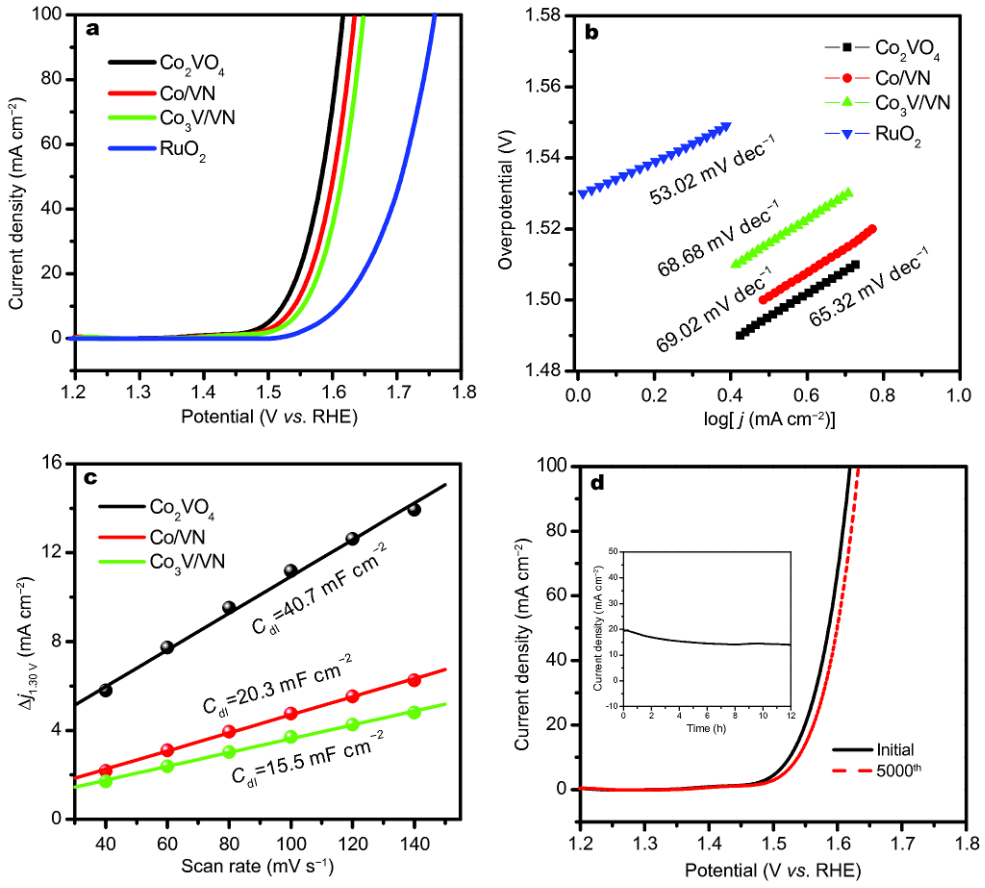

Figure 5 (a) LSV curves for Co_2VO_4, Co/VN, Co_3V/VN and commercial RuO_2 with *iR* compensation; (b) *iR* compensation Tafel plots for Co_2VO_4, Co/VN, Co_3V/VN and RuO_2; (c) the capacitive current at 1.30 V of Co_2VO_4, Co/VN and Co_3V/VN; (d) polarization data for the Co/VN sample initially and after 5000 CV. The inset in (d) is the dependence of the current density for Co_2VO_4 at 1.55 V for 12 h.

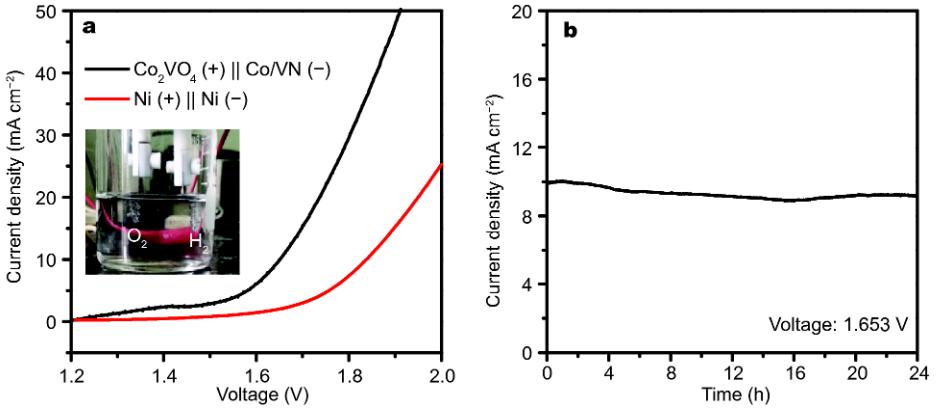

Figure 6 (a) LSV curves of the Co_2VO_4||Co/VN water splitting system in 1 mol L^{-1} KOH. The inset in (a) is a photograph of the two electrode device. (b) Chronoamperometry of water electrolysis using the Co_2VO_4||Co/VN two electrode water splitting system at 1.653 V.

trode system was assembled by using Co_2VO_4 as anode and Co/VN as cathode in 1.0 mol L^{-1} KOH for overall water splitting (Co_2VO_4||Co/VN). Fig. 6a shows that the cell can achieve a current density of 10 mA cm^{-2} at the cell voltage of 1.65 V. In addition, the Co_2VO_4||Co/VN system also shows good durability upon long-term op-

eration for 24 h in the alkaline solution (Fig. 6b). A "slightly ascending, then stable" trend is observed in the test. We could attribute this electrocatalytic stability to the partial dissolution of the peripheral part, which might expose a sufficient number of active sites and thereby enhance the electrocatalytic activity. The results highlight the potential of the Co-V bimetal-based catalyst for cost-effective and energy-efficient water electrolysis.

CONCLUSION

In summary, we have developed a robust route toward the Co-V bimetal-based nanoplates by the calcination of the $Co_2V_2O_7{\cdot}xH_2O$ precursor. The components and micro-structure of the catalysts could be easily tuned by simply regulating the calcination parameters, and the Co_2VO_4, Co/VN and Co_3V/VN can be selectively obtained. The catalysts exhibited good and structure-related performance for HER and OER. The Co/VN showed good performance for HER and the Co_2VO_4 is suitable catalyst for OER. When the Co_2VO_4 and Co/VN were used as the cathode and anode respectively in a two-electrode system, the cell needs a voltage of 1.65 V to achieve 10 mA cm^{-2} together with good stability. This work would be promising for constructing Co-V bimetal-based catalysts for the catalytic application.

Received 15 August 2017; accepted 7 September 2017; published online 7 November 2017

1 Mendoza-Sánchez B, Gogotsi Y. Synthesis of two-dimensional materials for capacitive energy storage. Adv Mater, 2016, 28: 6104–6135
2 Morales-Guio CG, Stern LA, Hu X. Nanostructured hydrotreating catalysts for electrochemical hydrogen evolution. Chem Soc Rev, 2014, 43: 6555–6569
3 Lu S, Zhuang Z. Electrocatalysts for hydrogen oxidation and evolution reactions. Sci China Mater, 2016, 59: 217–238
4 Luo J, Im JH, Mayer MT, *et al.* Water photolysis at 12.3% efficiency *via* perovskite photovoltaics and Earth-abundant catalysts. Science, 2014, 345: 1593–1596
5 Zhang Y, Shao Q, Pi Y, *et al.* A cost-efficient bifunctional ultrathin nanosheets array for electrochemical overall water splitting. Small, 2017, 13: 1700355
6 Tahir M, Pan L, Idrees F, *et al.* Electrocatalytic oxygen evolution reaction for energy conversion and storage: a comprehensive review. Nano Energ, 2017, 37: 136–157
7 Jiao Y, Zheng Y, Jaroniec M, *et al.* Design of electrocatalysts for oxygen- and hydrogen-involving energy conversion reactions. Chem Soc Rev, 2015, 44: 2060–2086
8 Ou G, Fan P, Zhang H, *et al.* Large-scale hierarchical oxide nanostructures for high-performance electrocatalytic water splitting. Nano Energ, 2017, 35: 207–214
9 Kuai L, Geng J, Chen C, *et al.* A reliable aerosol-spray-assisted approach to produce and optimize amorphous metal oxide catalysts for electrochemical water splitting. Angew Chem Int Ed, 2014, 53: 7547–7551
10 Li X, Zhang L, Huang M, *et al.* Cobalt and nickel selenide nanowalls anchored on graphene as bifunctional electrocatalysts for overall water splitting. J Mater Chem A, 2016, 4: 14789–14795
11 Zhang J, Zhao Z, Xia Z, *et al.* A metal-free bifunctional electrocatalyst for oxygen reduction and oxygen evolution reactions. Nat Nanotech, 2015, 10: 444–452
12 Tang C, Gan L, Zhang R, *et al.* Ternary $Fe_xCo_{1-x}P$ nanowire array as a robust hydrogen evolution reaction electrocatalyst with Pt-like activity: experimental and theoretical insight. Nano Lett, 2016, 16: 6617–6621
13 Zhang YX, Chang C, Teng F, *et al.* Defect-engineered ultrathin δ-MnO_2 nanosheet arrays as bifunctional electrodes for efficient overall water splitting. Adv Energy Mater, 2017, 7: 1700005
14 Zou X, Zhang Y. Noble metal-free hydrogen evolution catalysts for water splitting. Chem Soc Rev, 2015, 44: 5148–5180
15 Yan Y, Xia BY, Zhao B, *et al.* A review on noble-metal-free bifunctional heterogeneous catalysts for overall electrochemical water splitting. J Mater Chem A, 2016, 4: 17587–17603
16 Qu Y, Shao M, Shao Y, *et al.* Ultra-high electrocatalytic activity of VS_2 nanoflowers for efficient hydrogen evolution reaction. J Mater Chem A, 2017, 5: 15080–15086
17 Wu A, Tian C, Yan H, *et al.* Hierarchical MoS_2@MoP core-shell heterojunction electrocatalysts for efficient hydrogen evolution reaction over a broad pH range. Nanoscale, 2016, 8: 11052–11059
18 Liu T, Liu D, Qu F, *et al.* Enhanced electrocatalysis for energy-efficient hydrogen production over cop catalyst with none-lectroactive Zn as a promoter. Adv Energ Mater, 2017, 7: 1700020
19 Zeng M, Wang H, Zhao C, *et al.* 3D graphene foam-supported cobalt phosphate and borate electrocatalysts for high-efficiency water oxidation. Sci Bull, 2015, 60: 1426–1433
20 Tang C, Zhang R, Lu W, *et al.* Fe-doped CoP nanoarray: a monolithic multifunctional catalyst for highly efficient hydrogen generation. Adv Mater, 2017, 29: 1602441
21 Ma M, Zhu G, Xie F, *et al.* Homologous catalysts based on fe-doped cop nanoarrays for high-performance full water splitting under benign conditions. ChemSusChem, 2017, 10: 3188–3192
22 Zhang X, Gu W, Wang E. Wire-on-flake heterostructured ternary $Co_{0.5}Ni_{0.5}P$/CC: an efficient hydrogen evolution electrocatalyst. J Mater Chem A, 2017, 5: 982–987
23 Tang C, Cheng N, Pu Z, *et al.* NiSe nanowire film supported on nickel foam: an efficient and stable 3D bifunctional electrode for full water splitting. Angew Chem Int Ed, 2015, 54: 9351–9355
24 Jia X, Zhao Y, Chen G, *et al.* Ni_3FeN nanoparticles derived from ultrathin NiFe-layered double hydroxide nanosheets: an efficient overall water splitting electrocatalyst. Adv Energ Mater, 2016, 6: 1502585
25 Yan H, Tian C, Wang L, *et al.* Phosphorus-modified tungsten nitride/reduced graphene oxide as a high-performance, non-noble-metal electrocatalyst for the hydrogen evolution reaction. Angew Chem Int Ed, 2015, 54: 6325–6329
26 Zhang L, Xie L, Ma M, *et al.* Co-based nanowire films as complementary hydrogen- and oxygen-evolving electrocatalysts in neutral electrolyte. Catal Sci Technol, 2017, 7: 2689–2694
27 Liao L, Wang S, Xiao J, *et al.* A nanoporous molybdenum carbide nanowire as an electrocatalyst for hydrogen evolution reaction. Energ Environ Sci, 2014, 7: 387–392
28 Zhang F, Shi Y, Xue T, *et al. In situ* electrochemically converting Fe_2O_3-$Ni(OH)_2$ to $NiFe_2O_4$-NiOOH: a highly efficient electrocatalyst towards water oxidation. Sci China Mater, 2017, 60: 324–

334
29 Zhao Y, Jia X, Chen G, *et al.* Ultrafine NiO nanosheets stabilized by TiO_2 from monolayer NiTi-LDH precursors: an active water oxidation electrocatalyst. J Am Chem Soc, 2016, 138: 6517–6524
30 Wang J, Cui W, Liu Q, *et al.* Recent progress in cobalt-based heterogeneous catalysts for electrochemical water splitting. Adv Mater, 2016, 28: 215–230
31 Chen Z, Zhao H, Zhang J, *et al.* IrNi nanoparticle-decorated flower-shaped $NiCo_2O_4$ nanostructures: controllable synthesis and enhanced electrochemical activity for oxygen evolution reaction. Sci China Mater, 2017, 60: 119–130
32 Hang L, Sun Y, Men D, *et al.* Hierarchical micro/nanostructured C doped Co/Co_3O_4 hollow spheres derived from $PS@Co(OH)_2$ for the oxygen evolution reaction. J Mater Chem A, 2017, 5: 11163–11170
33 Artero V, Chavarot-Kerlidou M, Fontecave M. Splitting water with cobalt. Angew Chem Int Ed, 2011, 50: 7238–7266
34 Lin Y, Pan Y, Zhang J. CoP nanorods decorated biomass derived N, P co-doped carbon flakes as an efficient hybrid catalyst for electrochemical hydrogen evolution. Electrochim Acta, 2017, 232: 561–569
35 Yang L, Yu J, Wei Z, *et al.* Co-N-doped MoO_2 nanowires as efficient electrocatalysts for the oxygen reduction reaction and hydrogen evolution reaction. Nano Energ, 2017
36 Tabassum H, Guo W, Meng W, *et al.* Hydrogen evolution: metal-organic frameworks derived cobalt phosphide architecture encapsulated into B/N Co-doped graphene nanotubes for all pH value electrochemical hydrogen evolution. Adv Energ Mater, 2017
37 Feng JX, Xu H, Dong YT, *et al.* Efficient hydrogen evolution electrocatalysis using cobalt nanotubes decorated with titanium dioxide nanodots. Angew Chem Int Ed, 2017, 56: 2960–2964
38 Peng X, Hu L, Wang L, *et al.* Vanadium carbide nanoparticles encapsulated in graphitic carbon network nanosheets: a high-efficiency electrocatalyst for hydrogen evolution reaction. Nano Energ, 2016, 26: 603–609
39 Shi H, Liang H, Ming F, *et al.* Efficient overall water-splitting electrocatalysis using lepidocrocite VOOH hollow nanospheres. Angew Chem Int Ed, 2017, 56: 573–577
40 Xing M, Kong LB, Liu MC, *et al.* Cobalt vanadate as highly active, stable, noble metal-free oxygen evolution electrocatalyst. J Mater Chem A, 2014, 2: 18435–18443
41 Zhang J, Yuan B, Cui S, *et al.* Facile synthesis of 3D porous $Co_3V_2O_8$ nanoroses and 2D $NiCo_2V_2O_8$ nanoplates for high performance supercapacitors and their electrocatalytic oxygen evolution reaction properties. Dalton Trans, 2017, 46: 3295–3302
42 Shen FC, Wang Y, Tang YJ, *et al.* CoV_2O_6-V_2O_5 coupled with porous N-doped reduced graphene oxide composite as a highly efficient electrocatalyst for oxygen evolution. ACS Energ Lett, 2017, 2: 1327–1333
43 Hyun S, Ahilan V, Kim H, *et al.* The influence of $Co_3V_2O_8$ morphology on the oxygen evolution reaction activity and stability. Electrochem Commun, 2016, 63: 44–47
44 Shang X, Yan KL, Rao Y, *et al. In situ* cathodic activation of V-incorporated Ni_xS_y nanowires for enhanced hydrogen evolution. Nanoscale, 2017, 9: 12353–12363
45 Fan K, Chen H, Ji Y, *et al.* Nickel-vanadium monolayer double hydroxide for efficient electrochemical water oxidation. Nat Commun, 2016, 7: 11981
46 Lettenmeier P, Wang L, Golla-Schindler U, *et al.* Nanosized IrO_x-Ir catalyst with relevant activity for anodes of proton exchange membrane electrolysis produced by a cost-effective procedure. Angew Chem Int Ed, 2016, 55: 742–746
47 Baudrin E. Synthesis and electrochemical properties of cobalt vanadates *vs.* lithium. Solid State Ion, 1999, 123: 139–153
48 Wu F, Yu C, Liu W, *et al.* Large-scale synthesis of $Co_2V_2O_7$ hexagonal microplatelets under ambient conditions for highly reversible lithium storage. J Mater Chem A, 2015, 3: 16728–16736
49 Peng X, Wang L, Hu L, *et al. In situ* segregation of cobalt nanoparticles on VN nanosheets *via* nitriding of $Co_2V_2O_7$ nanosheets as efficient oxygen evolution reaction electrocatalysts. Nano Energ, 2017, 34: 1–7
50 Huang K, Bi K, Liang C, *et al.* Novel VN/C nanocomposites as methanol-tolerant oxygen reduction electrocatalyst in alkaline electrolyte. Sci Rep, 2015, 5: 11351
51 Zhao D, Cui Z, Wang S, *et al.* VN hollow spheres assembled from porous nanosheets for high-performance lithium storage and the oxygen reduction reaction. J Mater Chem A, 2016, 4: 7914–7923
52 Zhu C, Liu Z, Wang J, *et al.* Novel Co_2VO_4 anodes using ultralight 3D metallic current collector and carbon sandwiched structures for high-performance Li-ion batteries. Small, 2017, 13: 1701260
53 Zhang S, Ni B, Li H, *et al.* Cobalt carbonate hydroxide superstructures for oxygen evolution reactions. Chem Commun, 2017, 53: 8010–8013
54 Zhao Y, Liu J, Liu C, *et al.* Amorphous CuPt alloy nanotubes induced by $Na_2S_2O_3$ as efficient catalysts for the methanol oxidation reaction. ACS Catal, 2016, 6: 4127–4134
55 García-Contreras MA, Fernández-Valverde SM, Vargas-García JR. Pt, PtCo and PtNi electrocatalysts prepared by mechanical alloying for the oxygen reduction reaction in 0.5 M H_2SO_4. Int J Hydrogen Energy, 2008, 33: 6672–6680
56 Liu YR, Shang X, Gao WK, *et al.* Ternary CoS_2/MoS_2/RGO electrocatalyst with CoMoS phase for efficient hydrogen evolution. Appl Surf Sci, 2017, 412: 138–145
57 Yang Y, Xu X, Wang X. Synthesis of Mo-based nanostructures from organic-inorganic hybrid with enhanced electrochemical for water splitting. Sci China Mater, 2015, 58: 775–784
58 Kibsgaard J, Jaramillo TF, Besenbacher F. Building an appropriate active-site motif into a hydrogen-evolution catalyst with thiomolybdate $[Mo_3S_{13}]^{(2-)}$ clusters. Nat Chem, 2014, 6: 248–253
59 Chen P, Xu K, Fang Z, *et al.* Metallic Co_4N porous nanowire arrays activated by surface oxidation as electrocatalysts for the oxygen evolution reaction. Angew Chem Int Ed, 2015, 54: 14710–14714
60 Yan KL, Shang X, Li Z, *et al.* Ternary mixed metal Fe-doped $NiCo_2O_4$ nanowires as efficient electrocatalysts for oxygen evolution reaction. Appl Surf Sci, 2017, 416: 371–378
61 Yan KL, Shang X, Gao WK, *et al.* Ternary $MnO_2/NiCo_2O_4$/NF with hierarchical structure and synergistic interaction as efficient electrocatalysts for oxygen evolution reaction. J Alloys Compd, 2017, 719: 314–321

Acknowledgements This work was supported by the Key Program Projects of the National Natural Science Foundation of China (21631004), the National Natural Science Foundation of China (21601055, 21571054 and 21401048), the Natural Science Foundation of Heilongjiang Province (B2017008), and Heilongjiang University Excellent Youth Foundation.

Author contributions Fu H and Tian C designed and engineered this work; Xiao Y carried out the experiments. Tian C, Xiao Y and Fu H wrote this paper. All authors contributed to the general discussion.

Conflict of interest The authors declare that they have no conflict of interest.

Supplementary information Experimental details and supporting data are available in the online version of the paper.

Yinglu Xiao received her BSc degree from Harbin University in 2015. She is currently a master candidate at Heilongjiang University under the guidance of Profs. Chungui Tian and Honggang Fu. Her research is focused on the design and synthesis of vanadium-based catalysts for HER and OER.

Chungui Tian received his BSc degree in 1997 from Inner Mongolia University for Nationalities. In 2004 and 2007, he received his MSc and PhD degrees both from Northeast Normal University under the guidance of Prof. Enbo Wang. Then, he joined Heilongjiang University as a lecturer. He became an assistant professor and a full professor in 2009 and 2014, respectively. His research interests focus on designed synthanis and electrocatalytic application of W (Mo,V)-based materials.

Honggang Fu received his BSc degree in 1984 and MSc degree in 1987 from Jilin University, China. He joined Heilongjiang University as an assistant professor in 1988. In 1999, he received his PhD degree from Harbin Institute of Technology, China. He became a full professor in 2000. Currently, he is Cheung Kong Scholar Professor. His interests focus on the oxide-based nanomaterials for solar energy conversion and photocatalysis, the carbon-based nanomaterials for energy conversion and storage, and electrocatalysis.

Co-V双金属基纳米片用于有效电催化全解水

肖英璐, 田春贵*, 田玫, 吴爱平, 闫海静, 陈聪芳, 王蕾, 焦艳清, 付宏刚*

摘要 开发高效的全解水催化剂对于使用清洁水为原料制氢十分必要. 本文设计合成了钴-钒基双金属纳米片用作分解水的有效催化剂. 合成中采用$Co_2V_2O_7{\cdot}xH_2O$作为前驱体, 在氨气氛围下可控热处理获得组成可调的钴-钒基双金属(Co_2VO_4和Co/VN)纳米片. 电化学测试结果表明Co-V双金属基催化剂可作为活性的产氧和产氢催化剂. Co/VN具有较好的HER性能, 起始电位为68 mV, 电流密度为10 mA cm^{-2}时电压为92 mV. 而Co_2VO_4具有较好的OER性能, 电流密度为10 mA cm^{-2}时电压为300 mV. 使用Co/VN和Co_2VO_4分别作为阴极和阳极构建两电极电解池, 当电压为1.65 V时, 电流密度即可达到10 mA cm^{-2}. 因此, 组分可调的Co-V双金属纳米片在催化领域中具有很好的应用

